PHOTONICS Research

Ultrafast and low-power optoelectronic infrared-to-visible upconversion devices

Zhao Shi,[1,†] He Ding,[2,†] Hao Hong,[3] Dali Cheng,[1] Kamran Rajabi,[1] Jian Yang,[2] Yongtian Wang,[2] Lai Wang,[1] Yi Luo,[1] Kaihui Liu,[3] and Xing Sheng[1,*]

[1]Department of Electronic Engineering and Beijing National Research Center for Information Science and Technology, Tsinghua University, Beijing 100084, China
[2]Beijing Engineering Research Center of Mixed Reality and Advanced Display, School of Optics and Photonics, Beijing Institute of Technology, Beijing 100081, China
[3]State Key Laboratory for Mesoscopic Physics, Collaborative Innovation Center of Quantum Matter, and School of Physics, Peking University, Beijing 100871, China
*Corresponding author: xingsheng@tsinghua.edu.cn

Received 3 June 2019; revised 4 August 2019; accepted 14 August 2019; posted 15 August 2019 (Doc. ID 368929); published 1 October 2019

Photon upconversion with transformation of low-energy photons to high-energy photons has been widely studied and especially applied in biomedicine for sensing, stimulation, and imaging. Conventional upconversion materials rely on nonlinear luminescence processes, suffering from long decay lifetime or high excitation power. Here, we present a microscale, optoelectronic infrared-to-visible upconversion device design that can be excited at low power (1–100 mW/cm^2). By manipulating device geometry, illumination position, and temperature, the device luminescence decay lifetime can be tuned from tens to hundreds of nanoseconds. Based on carrier transportation and circuit dynamics, theoretical models are established to understand the transient behaviors. Compared with other mechanisms, the optoelectronic upconversion approach demonstrates the shortest luminescence lifetime with the lowest required excitation power, owing to its unique photon–electron conversion process. These features are expected to empower the device with essential capabilities for versatile applications as high-performance light emitters.

https://doi.org/10.1364/PRJ.7.001161

1. INTRODUCTION

Photon upconversion is an anti-Stokes process that yields high-energy photons via absorbing low-energy ones [1–5], arousing tremendous interest in numerous applications including biomedicine [5], light emitters [6], energy harvesting [7–10], displays [11], and imaging [12–17]. Conventional upconversion techniques rely on nonlinear optical processes in materials like lanthanide/rare-earth based crystals [4,18–21], organic luminophores based on the triplet–triplet annihilation (TTA) [22–26], and inorganic quantum dot–quantum well (QD-QW)-based semiconductor nanostructures [27–29]. Stemming from the nonlinear energy transfer mechanisms, these approaches fundamentally require high power optical excitations (typically >1 W/cm^2 for lanthanides and QD-QW) or exhibit long luminescence lifetimes (typically >1 μs for lanthanides and TTA), and present low photostability as well [19,27,30,31].

To circumvent these challenges, recently we have developed a microscale infrared (IR)-to-visible optoelectronic upconversion device based on designed semiconductor heterostructures [32]. Fundamentally different from conventional mechanisms, such optoelectronic devices utilize photon-to-electron and electron-to-photon transitions for upconversion, showing visible luminescence linearly dependent on IR irradiation. As a result, the devices can be excited under a low-power excitation condition, demonstrating fast transient dynamics and high stability in biological environments. In this paper, we perform time-resolved photoluminescence (TRPL) measurements and theoretical analysis to further understand the transient behaviors of our designed optoelectronic upconversion devices. These devices exhibit geometrically dependent luminescence decay lifetimes (ranging from ~20 ns to ~200 ns), which can be well explained by the carrier transport and circuit dynamics within the devices. Finally, we compare the device performance with other upconversion approaches, clearly revealing the uniqueness of our optoelectronic upconversion strategy featuring both low-power excitation and fast dynamics.

2. RESULTS

Our optoelectronic upconversion device design based on single-crystalline, inorganic semiconductor heterostructures is illustrated in Fig. 1(a). With experimental details provided

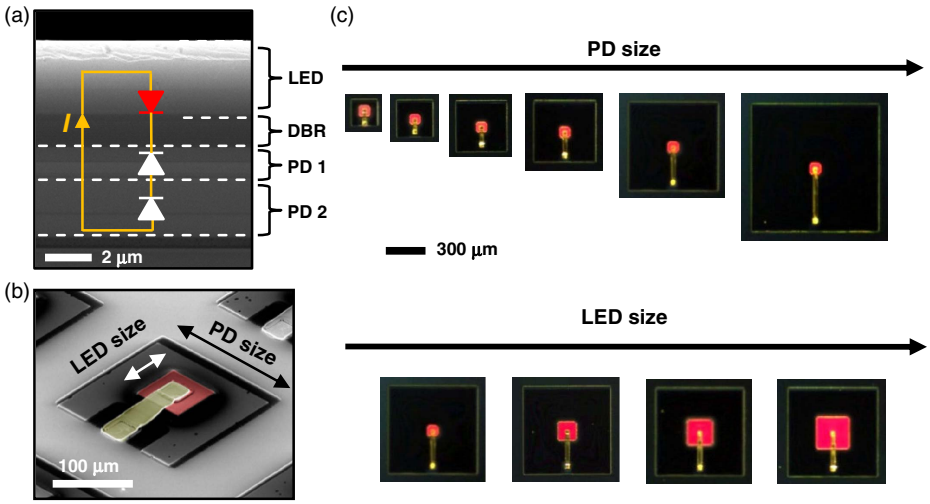

Fig. 1. (a) Cross-sectional scanning electron microscope (SEM) image of the optoelectronic upconversion device structure, including a red-emitting AlGaInP LED, a DBR, and a GaAs double-junction photodiode (DJPD), epitaxially grown on a GaAs substrate. The schematic of the corresponding circuit model is also shown, illustrating the upconversion mechanism. (b) Colorized SEM image (tilted view) of a fully fabricated device, showing designed LED (red color) and PD (gray color) components interconnected with metal wire (yellow color). (c) Top view, microscopic images of fabricated devices with different PD sizes (side length: 200 μm, 300 μm, 400 μm, 500 μm, 700 μm, 1000 μm, with a fixed LED size of 80 μm × 80 μm) or LED sizes (side length: 80 μm, 150 μm, 200 μm, 250 μm, with a fixed PD size of 700 μm × 700 μm) under the excitation of near-IR light (810 nm).

in our previous work [32], the multilayered structure includes an aluminum gallium indium phosphide (AlGaInP)-based red light-emitting diode (LED) (with a bandgap of around 1.9 eV, and an emitting peak at 630 nm), a distributed Bragg reflector (DBR) selectively reflecting red light, and a gallium arsenide (GaAs)-based double-junction photodiode (DJPD), all epitaxially grown on a lattice-matched GaAs substrate by metal organic chemical vapor deposition (MOCVD). As the circuit model illustrates, the GaAs PD collects near-IR light and produces photogenerated voltage and current, capable of driving the AlGaInP LED to emit red light. Lithographic processes define the device geometries and interconnection schemes, with a fully fabricated device example shown in Fig. 1(b). Devices with designed geometries can be fabricated with high yields in large-scale arrays. The designed device should ensure a large-enough PD area for sufficient IR absorption, so the LED size is limited. Therefore, the variation of the PD size (from 200 μm to 1000 μm) is more dramatic than that of the LED size (only from 80 μm to 250 μm). Figure 1(c) depicts devices with various LED and PD sizes, emitting red light (~630 nm) under near-IR illumination (~810 nm) with an incoherent light source. The absorption and emission spectra of these devices are only determined by the III–V semiconductors (AlGaInP and GaAs) and remain invariant for devices with different geometries. As demonstrated previously [32], these devices exhibit a linear upconversion response at IR illumination power above ~1 mW/cm^2, with an external quantum efficiency of ~1.5%.

As we demonstrated previously [32], our designed optoelectronic upconversion devices present a temporal response of nanoseconds, which is much faster compared to conventional lanthanide or organic-based nonlinear materials. This can be attributed to the extremely short carrier lifetime in III–V inorganic semiconductors, while the device time response is mainly limited by the interconnecting circuit. Thus, the transient response may be influenced by the device geometries. In Fig. 2, we study the TRPL behaviors for devices with varied LED and PD sizes. TRPL measurements are performed using a time-correlated single-photon counting (TCSPC) system with a time-synchronized femtosecond laser tuned to 800 nm (power density

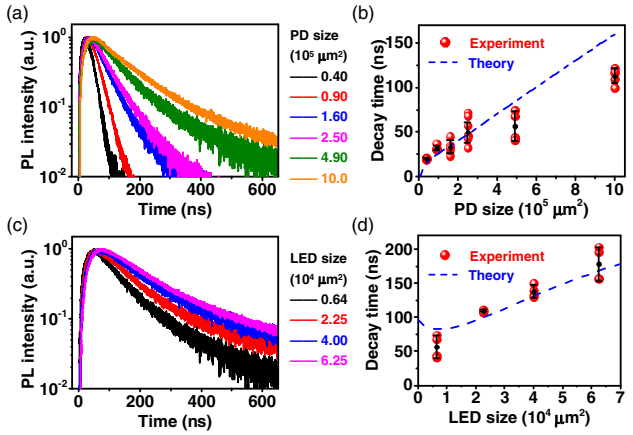

Fig. 2. (a) Measured TRPL decay curves for representative devices with different PD sizes (indicated in area) and a fixed LED size of 80 μm × 80 μm. (b) Measured PL decay time as a function of PD size (red dots, with error bars included), in comparison with the theoretically calculated curve (blue dashed line). (c) Measured TRPL decay curves for representative devices with different LED sizes (indicated in area) and a fixed PD size of 700 μm × 700 μm. (d) Measured PL decay time as a function of LED size (red dots, with error bars included), in comparison with the theoretically calculated curve (blue dashed line). For all curves, the maximum PL intensities are normalized to unity.

~500 mW/cm^2 for all devices) and a single-photon detector collecting luminescence signals at 630 nm. Measured TRPL decay curves for more than 20 devices with varied PD and LED sizes are respectively plotted in Figs. 2(a) and 2(c), with corresponding decay lifetimes summarized in Figs. 2(b) and 2(d). Because of the complicated carrier transport mechanisms, most PL decay curves exhibit multiple exponential decay processes. In our analysis, we only consider the initial decay including the decay process in which the PL intensity decreases from ~90% to ~10%. The rise times of all devices are relatively short (less than 10 ns), while the fall times (decay times) are longer and present a clear dependence on the device geometries. Specifically, the measured decay lifetimes monotonically increase with LED and PD sizes. When the device sizes vary from 80 μm × 80 μm to 1000 μm × 1000 μm (side length of LED: 80 μm, 150 μm, 200 μm, 250 μm; side length of PD: 200 μm, 300 μm, 400 μm, 500 μm, 700 μm, 1000 μm), measured decay lifetimes can be tuned between ~20 ns and ~200 ns.

To theoretically understand the transient response of these optoelectronic upconversion devices, here we establish a physical model to analyze the carrier generation, transport, and recombination behaviors. In particular, the upconversion luminescence lifetime of these devices depends on the temporal response of semiconductor materials and circuits, which generally involves photogenerated carrier generation and recombination, nonequilibrium carrier transportation, and resistance-capacitance (RC) delay in the circuit. In III–V-based devices, the carrier lifetime is normally less than 10 ns, and much shorter in highly doped materials (<1 ns), because of the high generation and recombination rates [33]. In addition, the carrier transportation in the vertical direction is also very fast due to the effect of the built-in electric field in p-n junctions and has a much smaller transportation length (<10 μm) compared to that in the lateral direction (>100 μm). Therefore, the device response time (τ_{total}) can be mainly ascribed to the combination of lateral carrier transportation time (τ_{trans}) and RC circuit delay (τ_{RC}) [34],

$$\tau_{\text{total}} = \sqrt{\tau_{\text{trans}}^2 + \tau_{\text{RC}}^2}. \quad (1)$$

It can be clearly seen that the collection of nonequilibrium carriers (i.e., transportation) is strongly influenced by the device geometry, and lumped parameters of these devices (resistance R and capacitance C) also directly correlate with the junction area. In other words, both τ_{RC} and τ_{trans} vary with the dimensions of devices. When these two parts are close to zero, carrier lifetimes inside the devices will be dominant. Detailed analysis is provided in Appendix A. The calculated PL decay lifetimes (τ_{total}) as functions of device geometries (in dashed line) are also plotted in Figs. 2(b) and 2(d), with results in good accordance with experimental results (in red dots). Shown in our theoretical model, the contributions of the RC delay time and the transportation time are dominant in different ranges of device dimensions, respectively. Therefore, an inflection point and a minimum point exist in the theoretical curves in Figs. 2(b) and 2(d), respectively. The remaining deviation may be associated with the simplified device layout we implement in our model, compared to the realistic, complicated device epitaxial structure. Nevertheless, such a simplified model is able to quantitatively predict the upconversion lifetimes of our devices, and provides possibilities of rational lifetime engineering for various potential applications.

Figure 3 further analyzes the relationship between the upconversion device lifetimes and device dimensions. As shown in Fig. 3(a), here we carry out TRPL measurements by focusing a small laser spot (around 20 μm in diameter) on the device surface, with varied positions from P_1 to P_4. We chose a device with a PD size of 300 μm × 300 μm to investigate the influence of the illumination position on the PL decay. TRPL results are measured and plotted in Fig. 3(b), showing rise and fall times increasing with the distance between the incident location and the edge of the LED. Figure 3(c) plots the measured PL decay lifetime as a function of this incident distance, in comparison with the calculated curve. It should be noted that results in Fig. 3 are different from those in Fig. 2, since illumination patterns are varied. The increased PL lifetimes with the incident distance can be attributed to the photogenerated carrier transportation in the lateral direction on the PD surface.

As seen in our theoretical analysis, many parameters associated with carrier dynamics in upconversion devices are temperature sensitive, leading to a thermally dependent transient response. Figure 4 shows measured TRPL results for a representative upconversion device at temperatures varying from 0°C to 80°C. The results indicate accelerated PL decays with increased temperatures. The decreasing trend of upconversion lifetime here is similar to materials based on other energy transfer processes like lanthanides [35], TTA-based materials [36], and other fluorophores [37]. However, the underlining mechanisms of temperature dependence are different. In conventional energy-transfer-based upconversion processes, the reduced PL decay lifetimes with increased temperatures are

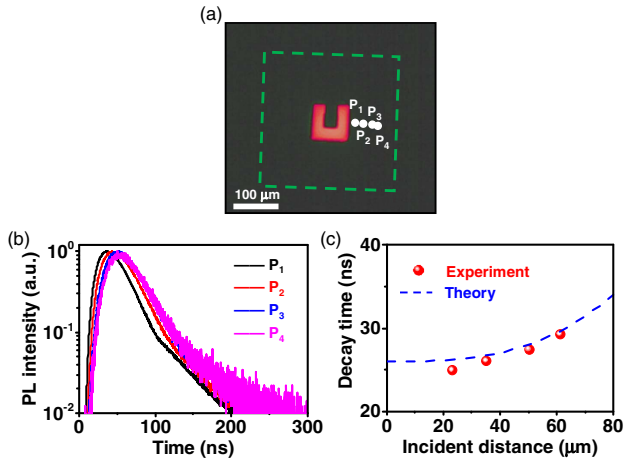

Fig. 3. (a) Microscopic image (top view) of an upconversion device emitting red light under near-IR illumination (LED size, 80 μm × 80 μm; and PD size, 300 μm × 300 μm). The green dashed square represents the edge of PD, and the white dots indicate the incident positions of focused IR laser spot. P_1 – P_4 indicate four different incident points. (b) Measured TRPL decay curves of the upconversion device with different incident positions on the PD. (c) Measured PL decay time (red dots) as a function of the distance between the incident laser spot (P_1 – P_4) and the nearest edge of the LED, in comparison with the theoretically calculated curve (blue dashed line).

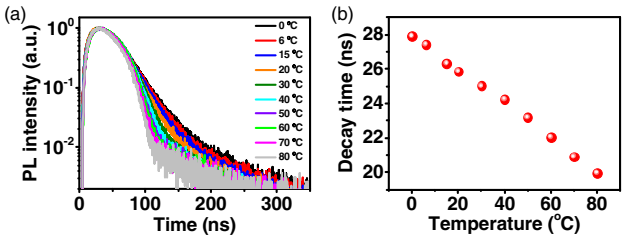

Fig. 4. (a) Measured TRPL decay curves for a representative upconversion device (LED size, 80 μm × 80 μm; PD size, 300 μm × 300 μm) at different temperatures. (b) Measured PL decay time (red dots) as a function of temperature.

due to thermally activated nonradiative decay [35–37]. By contrast, the transient behaviors in our optoelectronic upconversion design are dominated by the carrier transportation and the circuit RC delay [Eq. (1)], in which multiple parameters are thermally dependent and contribute to the influence of temperature on the upconversion lifetime.

3. DISCUSSION

With the unique process of converting low-energy photons to high-energy ones and their potential uses in many fields, IR-to-visible upconversion materials and systems have been considerably studied. In Fig. 5(a), we overview the operational principles of several representative upconversion strategies, including lanthanide-based, TTA-based, and QD-QW-based materials and structures, in comparison with our developed optoelectronic upconversion devices. Unlike these conventional strategies based on energy transfer processes within highly "localized" electronic structures, our device utilizes "photons to free electrons" and "free electrons to photons" to upconvert IR light to visible. As presented in this paper as well as in our previous report [32], such a unique concept enables linear energy conversion responses, requiring low-power excitation and exhibiting fast transient dynamics. Figure 5(b) summarizes typical excitation power densities and decay lifetimes for different upconversion strategies. Lanthanide-based upconversion materials typically require an excitation power density from ~10^3 mW/cm^2 to ~10^9 mW/cm^2 [4,18–21], suggesting that a high-power IR laser source should be applied for excitation and heating effects must be taken into consideration for practical uses. In addition, the decay lifetime is relatively long and within the range from microseconds (~10^{-6} s) to milliseconds (~10^{-3} s), attributed to the energy transition of 4f-electrons [17]. The minimum excitation power for TTA-based upconversion materials is relatively lower (from ~1 mW/cm^2 to ~10^6 mW/cm^2) due to their higher conversion efficiencies, but their decay lifetime is similar to lanthanides (μs–ms) [22–26,31,38]. In addition, TTA-based upconversion can also be achieved by hybrid organic–inorganic structures for high performance in multiple applications [39–41].

Similar to our optoelectronic upconversion devices, QD-QW-based structures exhibit shorter lifetimes (within nanoseconds), because of faster carrier generation and recombination rates within III–V- and II–IV-based inorganic semiconductors [27–29]. Similar to lanthanide-based upconversion, the

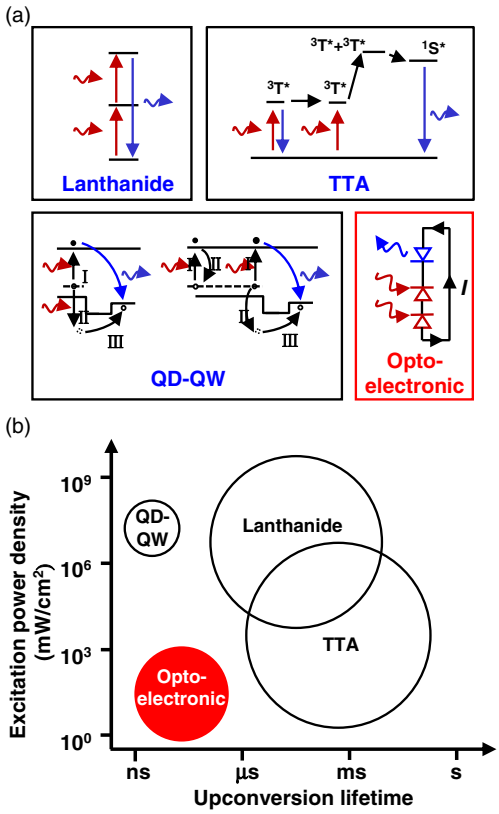

Fig. 5. (a) Schematic overview of representative upconversion mechanisms, including lanthanide-based, TTA-based, QD-QW-based, and our optoelectronic-device-based upconversion designs. (b) A summary of upconversion lifetimes and typical excitation power densities for four different mechanisms.

required excitation power is much higher (>10^6 mW/cm^2) due to the nature of nonlinear processes and associated low conversion efficiencies. Different from these conventional materials and structures, the distinct optoelectronic upconversion process in our devices allows for a short lifetime and a low excitation power density at the same time. The required excitation power density of our upconversion devices can be as low as ~1 mW/cm^2, and the linear operation can be realized at ~10 mW/cm^2 (10% of the standard one-sun illumination) by using a low-power, incoherent LED lamp. Although it is known that carrier transport processes are also power dependent because of various nonlinear mechanisms [42], the PL decay lifetimes are similar at different powers within our study range (1–1000 mW/cm^2). A tunable lifetime (from ~20 ns to ~200 ns) can be achieved by altering the device dimensions. The quantum yield of these upconversion devices is around 1.5%, which is almost not affected by the excitation power. The losses are mainly from the low extraction efficiency of LEDs due to high refractive indices of III–V materials. It can be improved by effective optical optimizations such as surface treatment on LEDs [32].

4. CONCLUSION

In summary, we thoroughly analyze the luminescence lifetime of our optoelectronic upconversion devices with different

geometries, under different illuminating locations, and at different temperatures. Among existing technologies, our devices require the lowest excitation power and present the shortest decay lifetime, owing to the nature of linear energy conversion and the use of high-quality III–V semiconductors. Based on the mature integrated manufacturing of electronic devices, these upconversion devices can form large-scale arrays, with effective biocompatible encapsulation to avoid toxicity and inflammation. These arrays can be used for large-scope addressable biological stimulation, sensing, and imaging [32,43,44]. Such unique properties could make the devices suitable for potential applications in areas like high-throughput chemical sensing [45] and dynamic biological stimulations [46]. By further scaling down the device size to several micrometers or submicrometers, it is envisioned that even faster photon decay lifetimes and higher upconversion efficiencies can be achieved, as suggested in Fig. 2 and our previous work [32]. Other directions involve the study of the device performance under different chemical and biological environments. Collectively, results presented here suggest a viable pathway to design high-performance light emitters for various applications using optoelectronic upconversion.

APPENDIX A

1. CALCULATIONS

The lifetime (τ_{total}) of the optoelectronic upconversion device can be mainly ascribed to the combination of carrier transportation time (τ_{trans}) and RC circuit delay (τ_{RC}). The thin top layer of a DJPD section is heavily doped as the charge-neutral region, in which the carrier transportation is generally explained by diffusion. Therefore, τ_{trans} can be simplified to the diffusion time delay τ_{diff} in the following layer:

$$\tau_{\text{total}} = \sqrt{\tau_{\text{trans}}^2 + \tau_{\text{RC}}^2} = \sqrt{\tau_{\text{diff}}^2 + \tau_{\text{RC}}^2}. \tag{A1}$$

A. Diffusion Time Delay

The diffusion time delay τ_{diff} is the result of diffusion of nonequilibrium carriers induced by the carrier concentration gradient. Quantitatively, this transport mechanism can be analyzed by a one-dimensional diffusion model, in which a photogenerated constant carrier flow injects electrons into a bulk material at position $x = 0$ from time $t = 0$. At a specific time t, the distribution of carriers is calculated by solving the equation

$$\frac{\partial n}{\partial t} = D\frac{\partial^2 n}{\partial^2 x}, \tag{A2}$$

with the boundary conditions

$$\begin{cases} n(x,0) = 0 \\ -D\frac{\partial n}{\partial x}(0,t) = \frac{I_0}{\hbar\nu}, \\ n(\infty,t) = 0 \end{cases} \tag{A3}$$

where $n(x,t)$ is the carrier concentration, D is the diffusivity coefficient of the material (GaAs and GaInP), I_0 is incident excitation power density, and $\hbar\nu$ is the photon energy. The solution to this equation is

$$n(x,t) = \frac{I_0}{2\hbar\nu\sqrt{\pi D}}\int_0^t \frac{x\tau}{(t-\tau)^{3/2}}\exp\left[-\frac{x^2}{4D(t-\tau)}\right]\mathrm{d}\tau. \tag{A4}$$

Then, considering the differential equation,

$$\frac{\mathrm{d}x}{\mathrm{d}t} = v(x,t) = -\frac{1}{n(x,t)}D\frac{\partial n}{\partial x}, \tag{A5}$$

the function relationship between t and x is numerically determined, i.e., the required time t for an electron to travel the displacement of x is $t = t(x)$, which is solely determined by coefficient D.

As the thickness and diffusion coefficient of GaAs are larger and higher compared to GaInP in the optoelectronic upconversion device, for which the carriers in the PD tend to diffuse within GaAs layer, the diffusivity is set to $D = 200\ \text{cm}^2 \cdot \text{s}^{-1}$ (diffusivity of GaAs) in the diffusion-related calculation above.

In an actual upconversion device, nonequilibrium carriers at different places in the DJPD section diffuse through different distances to be collected by the LED section. Thus, the weighted average of these diffusion time results is calculated for devices with different dimensions, and is considered to be the overall diffusion time delay associated with device dimensions,

$$\tau_{\text{diff}} = \frac{\iint_S t[r_{\min}(x,y)]\mathrm{d}x\mathrm{d}y}{\iint_S \mathrm{d}x\mathrm{d}y}, \tag{A6}$$

where S denotes the area between the top LED and bottom DJPD, and $r_{\min}(x,y)$ is the shortest distance from point (x,y) to the edge of LED.

B. RC Time Constant Delay

The RC time constant delay τ_{RC} is mainly contributed by the junction capacitance in the device and the resistance in the circuit. The simplified small signal equivalent circuit of the upconversion device is used to analyze τ_{RC}, where the parallel resistance is ignored and the series resistance is merged (Fig. 6). In this circuit, τ_{RC} is calculated by

$$\tau_{\text{RC}} = \frac{R_{\text{total}}}{(C_{\text{jLED}}A_{\text{LED}})^{-1} + (C_{\text{jDJPD}}A_{\text{DJPD}})^{-1}}, \tag{A7}$$

where R_{total} is total series resistance, C_{jLED} and C_{jDJPD} are junction capacitances per unit area of LED and DJPD, respectively, and A_{LED} and A_{DJPD} are areas of LED and DJPD, respectively. The junction capacitances per unit area of LED and DJPD are acquired through theoretical calculation and experimental measurement (Table 1).

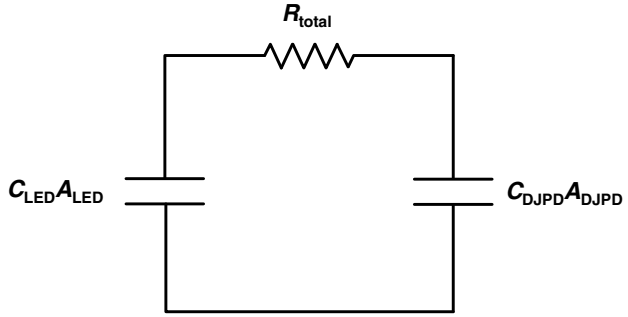

Fig. 6. Equivalent circuit of the IR-to-red optoelectronic upconversion device. The LED and DJPD are connected in series, and their capacitance and resistance render an RC delay.

Table 1. Theoretically Calculated and Experimentally Measured Junction Capacitance (per Unit Area) of LED and DJPD

C_{LED}, Calculated	C_{LED}, Measured	C_{DJPD}, Calculated	C_{DJPD}, Measured
3.3 fF/μm^2	3.4 fF/μm^2	0.60 fF/μm^2	0.70 fF/μm^2

In theoretical calculation, C_j of LED and single-junction PD is calculated by

$$C_j = C_{\text{depletion}} + C_{\text{diffusion}} = \sqrt{\frac{q\varepsilon_s}{2(V_i - V_a)}\frac{N_A N_D}{N_A + N_D}} + \frac{q^2 L}{kT}\frac{n_i^2}{N_A}\exp\left(\frac{qV_a}{kT}\right), \tag{A8}$$

where ε_s is the dielectric constant of the junction semiconductor material, N_A and N_D are doping concentrations, n_i is the intrinsic carrier density, L is the effective diffusion length [47], V_i is the intrinsic built-in voltage, and V_a is the applied forward voltage, which is determined as the operating voltage of the upconversion device (approximately 1.68 V) [32]. It should be also noted that the capacitance of a DJPD is half of a single-junction PD.

The capacitance–voltage (C–V) characteristics were measured with independent LEDs and DJPDs, which have the same structure with the two sections in upconversion device, respectively. The measured C–V characteristics are shown in Fig. 7, in which the capacitance is proportional to the device active area and shows a good accordance to calculated results of both DJPD and LED at the voltage of 1.68 V. Finally, for devices with different sizes of LED or DJPD, both C_j and R_{total} are calculated to obtain RC constant time delay.

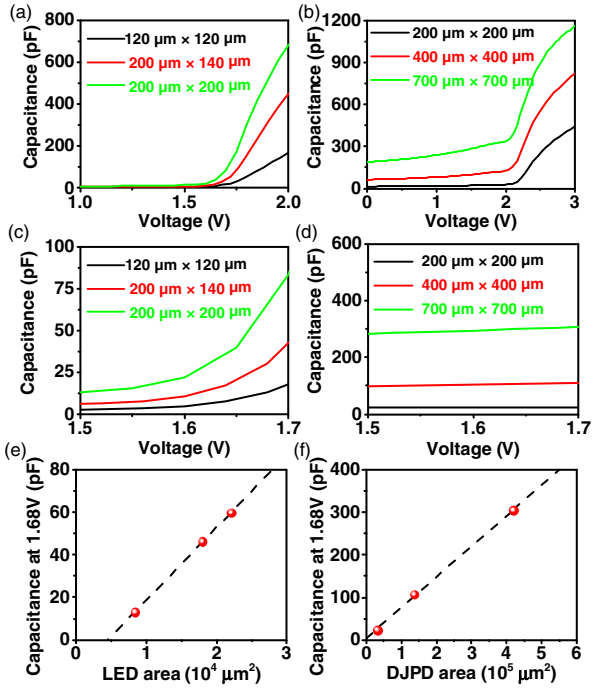

Fig. 7. Measured capacitance of (a) GaInP LED and (b) GaAs DJPD at 1 MHz. The designed device areas are indicated within the graph. (c) and (d) show zoomed-in details near the DC operating point (1.68 V) in (a) and (b), respectively. The capacitances at 1.68 V of (e) LED and (f) DJPD of different sizes (with different active areas) are measured (red dots), and the black dashed lines are linear fitting results.

C. Localized Excitation

In the localized excitation measurements as shown in Fig. 3, the incident light beam is concentrated in a diameter of ~20 μm. Under such circumstances, the diffusion time delay does not need to be averaged throughout the region, which can be directly obtained from $t = t(x)$. It can be assumed that the RC constant delay of localized excitation is constant because the junction capacitance is determined by the bandgap and photogenerated voltage over the junction.

2. MATERIALS AND METHODS

A. Optoelectronic Upconversion Materials and Structures

The optoelectronic upconversion material involves two parts (from top to bottom): (1) the LED structure [200 nm p-type GaP (C doping, 1×10^{20} cm^{-3}) contact layer, 2000 nm p-type GaP (Mg doping, 5×10^{18} cm^{-3}) window layer, 800 nm p-type AlInP (Mg doping, 1×10^{18} cm^{-3}) barrier layer, 200 nm AlInP/GaInP MQWs, 200 nm n-type AlInP (Si doping, 8×10^{17} cm^{-3}) barrier layer, 1200 nm n-type $Al_{0.5}In_{0.5}P$/$Al_{0.25}Ga_{0.25}In_{0.5}P$ (Si doping, 3×10^{18} cm^{-3}) DBR (12 loops), 700 nm n-type GaAs (Si doping, 6×10^{18} cm^{-3}) contact layer], (2) the PD 1 structure [30 nm n-type GaInP (Si doping, 2×10^{18} cm^{-3}) window layer, 100 nm n-type GaAs (Si doping, 2×10^{18} cm^{-3}) emitter layer, 450 nm p-type GaAs (Zn doping, 1×10^{17} cm^{-3}) base layer, 100 nm p-type $Al_{0.3}Ga_{0.7}As$ (Mg doping, 5×10^{18} cm^{-3}) BSF layer], the tunnel junction [11 nm p-type GaAs (C doping, 8×10^{19} cm^{-3}) and 11 nm n-type GaAs (Se doping, 9×10^{18} cm^{-3}) layer], the PD 2 structure [30 nm n-type $Al_{0.3}Ga_{0.7}As$ (Si doping, 2×10^{18} cm^{-3}) window layer, 100 nm n-type GaAs (Si doping, 2×10^{18} cm^{-3}) emitter layer, 1500 nm p-type GaAs (Zn doping, 1×10^{17} cm^{-3}) base layer, 100 nm p-type GaInP (Mg doping, 1×10^{18} cm^{-3}) BSF layer, 1000 nm p-type GaAs (Mg doping, 5×10^{18} cm^{-3}) contact layer]. An $Al_{0.95}Ga_{0.05}As$ sacrificial layer is added between device layers and GaAs substrate for releasing the devices from the substrate.

Furthermore, both the components of the upconversion structure (LED and PD) are also grown on the GaAs substrate independently, in order to perform the optical and electrical characterization.

B. Fabrication Process

A 500 nm thick SiO_2 is deposited via plasma-enhanced chemical vapor deposition (PECVD) method. Photolithographical patterning is followed by the removal of SiO_2 by buffered oxide etchant (BOE), GaP by $KOH/K_3[Fe(CN)_6]/H_2O$ (1:4:15, by weight), AlGaInP-based materials by HCl/H_3PO_4 (1:1, by volume), and GaAs-based materials by $H_3PO_4/H_2O_2/H_2O$

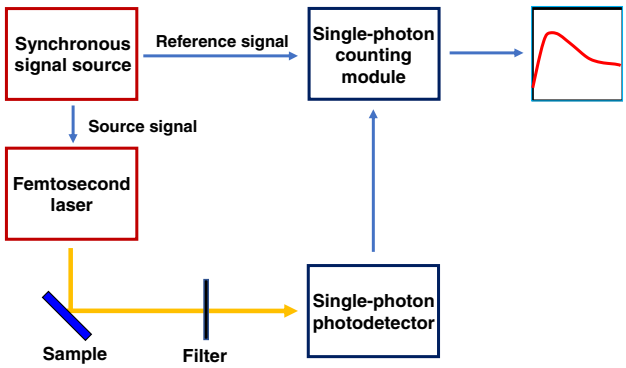

Fig. 8. Experimental setup for time-resolved photoluminescence measurements.

(3:1:25 by volume). The epoxy encapsulation with SU-8 and the following metal (Cr/Cu/Au) interconnects the LED and DJPD structures.

C. Experimental Measurements

TRPL measurements are taken using a TCSPC system. This self-built system consists of an ultrafast pulse laser from a coherent laser system (400 nm or 800 nm, 250 kHz, ~60 fs). The laser is driven by a synchronous signal source and tuned for 800 nm emission. In the measurements, the beam diameter of the laser is defocused or focused depending on the choice of irradiation on the entire device surface or localized, in which both the power densities are around 5 mW/mm^2. The upconversion emission (~630 nm) passes through a 700 nm short-pass filter with collection by a single-photon avalanche PD detector (TDA 200) combined with a TCSPC module (TimeHarp 260 PICO Single) to obtain the TRPL signal. The experimental setup is shown in Fig. 8.

The measurements under different temperatures employed a thermal electric cooler based on the Peltier effect and were calibrated by an IR thermometer. C–V characteristics of independent LEDs and DJPDs were measured using an Agilent 4284A LCR meter.

Funding. National Natural Science Foundation of China (NSFC) (51602172, 61874064); Beijing Institute of Technology Research Fund Program for Young Scholars (3040012221906); Beijing Innovation Center for Future Chips, Tsinghua University; Beijing National Research Center for Information Science and Technology (BNR2019ZS01005).

Disclosures. The authors declare that they have no competing interests.

†These authors contributed equally to this work.

REFERENCES

1. C. V. Raman, "A new radiation," Indian J. Phys. **2**, 387–398 (1928).
2. N. Bloembergen, "Solid state infrared quantum counters," Phys. Rev. Lett. **2**, 84–85 (1959).
3. F. Auzel, "Upconversion and anti-Stokes processes with f and d ions in solids," Chem. Rev. **104**, 139–174 (2004).
4. B. Zhou, B. Shi, D. Jin, and X. Liu, "Controlling upconversion nanocrystals for emerging applications," Nat. Nanotechnol. **10**, 924–936 (2015).
5. F. Zhang, *Photon Upconversion Nanomaterials* (Springer, 2015), Vol. **416**.
6. A. A. Kaminskii, H. J. Eichler, H. Rhee, K. Ueda, K. Oka, and H. Shibata, "New nonlinear-laser effects in $YbVO_4$ crystal: sesqui-octave Stokes and anti-Stokes comb generation and the cascaded self-frequency 'tripling' of $\chi^{(3)}$-Stokes components under a one-micron picosecond pumping," Laser Phys. **18**, 1546–1552 (2008).
7. T. Trupke, A. Shalav, B. S. Richards, P. Würfel, and M. A. Green, "Efficiency enhancement of solar cells by luminescent up-conversion of sunlight," Sol. Energy Mater. Sol. Cells **90**, 3327–3338 (2006).
8. W. Zou, C. Visser, J. A. Maduro, M. S. Pshenichnikov, and J. C. Hummelen, "Broadband dye-sensitized upconversion of near-infrared light," Nat. Photonics **6**, 560–564 (2012).
9. J. A. Briggs, A. C. Atre, and J. A. Dionne, "Narrow-bandwidth solar upconversion: case studies of existing systems and generalized fundamental limits," J. Appl. Phys. **113**, 124509 (2013).
10. M. A. Green and S. P. Bremner, "Energy conversion approaches and materials for high-efficiency photovoltaics," Nat. Mater. **16**, 23–34 (2016).
11. E. Downing, L. Hesselink, J. Ralston, and R. Macfarlane, "A three-color, solid-state, three-dimensional display," Science **273**, 1185–1189 (1996).
12. J. Zhou, Z. Liu, and F. Li, "Upconversion nanophosphors for small-animal imaging," Chem. Soc. Rev. **41**, 1323–1349 (2012).
13. F. Wang, D. Banerjee, Y. Liu, X. Chen, and X. Liu, "Upconversion nanoparticles in biological labeling, imaging, and therapy," Analyst **135**, 1839–1854 (2010).
14. D. K. Chatterjee, M. K. Gnanasammandhan, and Y. Zhang, "Small upconverting fluorescent nanoparticles for biomedical applications," Small **6**, 2781–2795 (2010).
15. F. Wang, R. Deng, J. Wang, Q. Wang, Y. Han, H. Zhu, X. Chen, and X. Liu, "Tuning upconversion through energy migration in core-shell nanoparticles," Nat. Mater. **10**, 968–973 (2011).
16. A. Lay, D. S. Wang, M. D. Wisser, R. D. Mehlenbacher, Y. Lin, M. B. Goodman, W. L. Mao, and J. A. Dionne, "Upconverting nanoparticles as optical sensors of nano- to micro-Newton forces," Nano Lett. **17**, 4172–4177 (2017).
17. Y. Liu, Y. Lu, X. Yang, X. Zheng, S. Wen, F. Wang, X. Vidal, J. Zhao, D. Liu, Z. Zhou, C. Ma, J. Zhou, J. A. Piper, P. Xi, and D. Jin, "Amplified stimulated emission in upconversion nanoparticles for super-resolution nanoscopy," Nature **543**, 229–233 (2017).
18. M. V. DaCosta, S. Doughan, Y. Han, and U. J. Krull, "Lanthanide upconversion nanoparticles and applications in bioassays and bioimaging: a review," Anal. Chim. Acta **832**, 1–33 (2014).
19. J. Zhao, Z. Lu, Y. Yin, C. McRae, J. A. Piper, J. M. Dawes, D. Jin, and E. M. Goldys, "Upconversion luminescence with tunable lifetime in $NaYF_4$:Yb, Er nanocrystals: role of nanocrystal size," Nanoscale **5**, 944–952 (2013).
20. Y.-F. Wang, G.-Y. Liu, L.-D. Sun, J.-W. Xiao, J.-C. Zhou, and C.-H. Yan, "Nd^{3+}-sensitized upconversion nanophosphors: efficient *in vivo* bioimaging probes with minimized heating effect," ACS Nano **7**, 7200–7206 (2013).
21. H. Qin, D. Wu, J. Sathian, X. Xie, M. Ryan, and F. Xie, "Tuning the upconversion photoluminescence lifetimes of $NaYF_4$:Yb^{3+}, Er^{3+} through lanthanide Gd^{3+} doping," Sci. Rep. **8**, 12683 (2018).
22. M. Wu, D. N. Congreve, M. W. B. Wilson, J. Jean, N. Geva, M. Welborn, T. Van Voorhis, V. Bulović, M. G. Bawendi, and M. A. Baldo, "Solid-state infrared-to-visible upconversion sensitized by colloidal nanocrystals," Nat. Photonics **10**, 31–34 (2015).
23. W. Wu, H. Guo, W. Wu, S. Ji, and J. Zhao, "Organic triplet sensitizer library derived from a single chromophore (BODIPY) with long-lived triplet excited state for triplet-triplet annihilation based upconversion," J. Org. Chem. **76**, 7056–7064 (2011).
24. Y. Y. Cheng, B. Fückel, T. Khoury, R. G. C. R. Clady, M. J. Y. Tayebjee, N. J. Ekins-Daukes, M. J. Crossley, and T. W. Schmidt, "Kinetic analysis of photochemical upconversion by triplet–triplet annihilation: beyond any spin statistical limit," J. Phys. Chem. Lett. **1**, 1795–1799 (2010).

25. W. Wu, J. Zhao, J. Sun, L. Huang, and X. Yi, "Red-light excitable fluorescent platinum(II) bis(aryleneethynylene) bis(trialkylphosphine) complexes showing long-lived triplet excited states as triplet photosensitizers for triplet–triplet annihilation upconversion," J. Mater. Chem. C **1**, 705–716 (2013).
26. A. Köhler and H. Bässler, "Triplet states in organic semiconductors," Mater. Sci. Eng. R **66**, 71–109 (2009).
27. Z. Deutsch, L. Neeman, and D. Oron, "Luminescence upconversion in colloidal double quantum dots," Nat. Nanotechnol. **8**, 649–653 (2013).
28. A. Teitelboim and D. Oron, "Broadband near-infrared to visible upconversion in quantum dot–quantum well heterostructures," ACS Nano **10**, 446–452 (2016).
29. Y. Chen and H. Liang, "Applications of quantum dots with upconverting luminescence in bioimaging," J. Photochem. Photobiol. B **135**, 23–32 (2014).
30. J. Bergstrand, Q. Liu, B. Huang, X. Peng, C. Würth, U. Resch-Genger, Q. Zhan, J. Widengren, H. Ågren, and H. Liu, "On the decay time of upconversion luminescence," Nanoscale **11**, 4959–4969 (2019).
31. C. Ye, L. Zhou, X. Wang, and Z. Liang, "Photon upconversion: from two-photon absorption (TPA) to triplet–triplet annihilation (TTA)," Phys. Chem. Chem. Phys. **18**, 10818–10835 (2016).
32. H. Ding, L. Lu, Z. Shi, D. Wang, L. Li, X. Li, Y. Ren, C. Liu, D. Cheng, H. Kim, N. C. Giebink, X. Wang, L. Yin, L. Zhao, M. Luo, and X. Sheng, "Microscale optoelectronic infrared-to-visible upconversion devices and their use as injectable light sources," Proc. Natl. Acad. Sci. USA **115**, 6632–6637 (2018).
33. E. F. Schubert, *Light-Emitting Diodes* (Cambridge University, 2006).
34. A. Rogalski and Z. Bielecki, "Detection of optical radiation," Bull. Pol. Acad. Sci. Tech. Sci. **52**, 43–66 (2006).
35. J. Zhang, B. Ji, G. Chen, and Z. Hua, "Upconversion luminescence and discussion of sensitivity improvement for optical temperature sensing application," Inorg. Chem. **57**, 5038–5047 (2018).
36. T. N. Singh-Rachford, J. Lott, C. Weder, and F. N. Castellano, "Influence of temperature on low-power upconversion in rubbery polymer blends," J. Am. Chem. Soc. **131**, 12007–12014 (2009).
37. H. Peng, M. I. J. Stich, J. Yu, L.-N. Sun, L. H. Fischer, and O. S. Wolfbeis, "Luminescent europium(III) nanoparticles for sensing and imaging of temperature in the physiological range," Adv. Mater. **22**, 716–719 (2010).
38. M. Mahboub, Z. Huang, and M. L. Tang, "Efficient infrared-to-visible upconversion with subsolar irradiance," Nano Lett. **16**, 7169–7175 (2016).
39. Z. Huang, X. Li, M. Mahboub, K. M. Hanson, V. M. Nichols, H. Le, M. L. Tang, and C. J. Bardeen, "Hybrid molecule–nanocrystal photon upconversion across the visible and near-infrared," Nano Lett. **15**, 5552–5557 (2015).
40. M. Mahboub, H. Maghsoudiganjeh, A. M. Pham, Z. Huang, and M. L. Tang, "Triplet energy transfer from PbS(Se) nanocrystals to rubrene: the relationship between the upconversion quantum yield and size," Adv. Funct. Mater. **26**, 6091–6097 (2016).
41. L. Nienhaus, M. Wu, V. Bulović, M. A. Baldo, and M. G. Bawendi, "Using lead chalcogenide nanocrystals as spin mixers: a perspective on near-infrared-to-visible upconversion," Dalton Trans. **47**, 8509–8516 (2018).
42. H. Ding, H. Hong, D. Cheng, Z. Shi, K. Liu, and X. Sheng, "Power- and spectral-dependent photon-recycling effects in a double-junction gallium arsenide photodiode," ACS Photon. **6**, 59–65 (2019).
43. R.-H. Kim, D.-H. Kim, J. Xiao, B. H. Kim, S.-I. Park, B. Panilaitis, R. Ghaffari, J. Yao, M. Li, Z. Liu, V. Malyarchuk, D. G. Kim, A.-P. Le, R. G. Nuzzo, D. L. Kaplan, F. G. Omenetto, Y. Huang, Z. Kang, and J. A. Rogers, "Waterproof AlInGaP optoelectronics on stretchable substrates with applications in biomedicine and robotics," Nat. Mater. **9**, 929–937 (2010).
44. J. Viventi, D.-H. Kim, L. Vigeland, E. S. Frechette, J. A. Blanco, Y.-S. Kim, A. E. Avrin, V. R. Tiruvadi, S.-W. Hwang, A. C. Vanleer, D. F. Wulsin, K. Davis, C. E. Gelber, L. Palmer, J. Van der Spiegel, J. Wu, J. Xiao, Y. Huang, D. Contreras, J. A. Rogers, and B. Litt, "Flexible, foldable, actively multiplexed, high-density electrode array for mapping brain activity *in vivo*," Nat. Neurosci. **14**, 1599–1605 (2011).
45. Y. Ding, H. Zhu, X. Zhang, J.-J. Zhu, and C. Burda, "Rhodamine B derivative-functionalized upconversion nanoparticles for FRET-based Fe^{3+}-sensing," Chem. Commun. **49**, 7797–7799 (2013).
46. S. Chen, A. Z. Weitemier, X. Zeng, L. He, X. Wang, Y. Tao, A. J. Y. Huang, Y. Hashimotodani, M. Kano, H. Iwasaki, L. K. Parajuli, S. Okabe, D. B. L. Teh, A. H. All, I. Tsutsui-Kimura, K. F. Tanaka, X. Liu, and T. J. McHugh, "Near-infrared deep brain stimulation via upconversion nanoparticle-mediated optogenetics," Science **359**, 679–684 (2018).
47. G. Friesen and H. A. Ossenbrink, "Capacitance effects in high-efficiency cells," Sol. Energ. Mat. Sol. C. **48**, 77–83 (1997).